

Design of Light-Driven Biocompatible and Biodegradable Microrobots Containing Mg-Based Metallic Glass Nanowires

Jinbiao Huang, Xiangyang Yu, Luyao Li, Wenxue Wang, Heting Zhang, Yu Zhang, Jian Zhu, and Jiang Ma*

Cite This: <https://doi.org/10.1021/acsnano.3c08277>

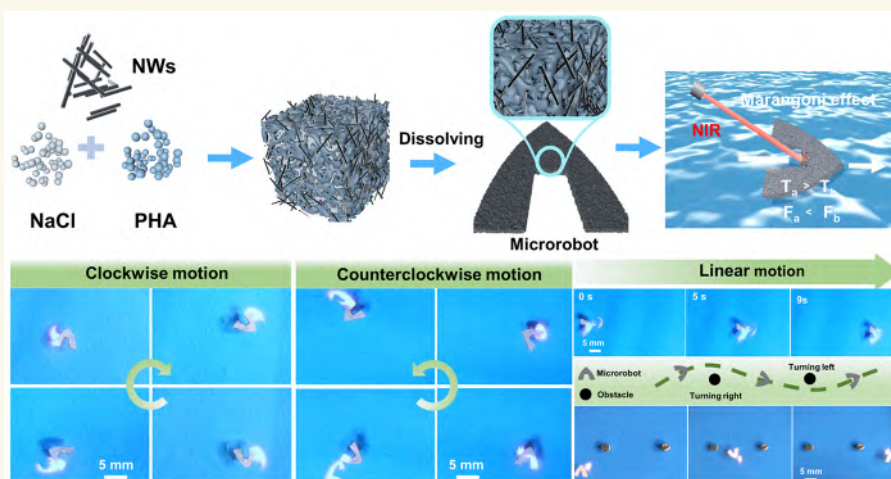
Read Online

ACCESS |

Metrics & More

Article Recommendations

Supporting Information



ABSTRACT: Light-driven microrobots capable of moving rapidly on water surfaces in response to external stimuli are widely used in a variety of fields, such as drug delivery, remote sampling, and biosensors. However, most light-driven microrobots use graphene and carbon nanotubes as photothermal materials, resulting in poor biocompatibility and degradability, which greatly limits their practical bioapplications. To address this challenge, a composition and microstructure design strategy with excellent photothermal properties suitable for the fabrication of light-driven microrobots was proposed in this work. The Mg-based metallic glass nanowires (Mg-MGNWs) were embedded with polyhydroxyalkanoates (PHA) to fabricate biocompatible and degradable microrobots with excellent photothermal effect and complex shapes. Consequently, the microrobot can be precisely driven by a near-infrared laser to achieve high efficiency and remote manipulation on the water surface for a long period of time, with a velocity of 9.91 mm/s at a power density of 2.0 W/cm². Due to the Marangoni effect, programmable and complex motions of the microrobot such as linear, clockwise, counterclockwise, and obstacle avoidance motions can be achieved. The biocompatible and degradable microrobot fabrication strategy could have great potential in the fields of environmental detection, targeted drug delivery, disease diagnosis, and detection.

KEYWORDS: microrobots, light-driven, Mg-based metallic glass nanowires, composition and microstructure design strategy, photothermal effect

1. INTRODUCTION

Bionic microrobot development is informed by animal adaptations to the diversity of locomotion modes found in nature. A range of bionic robots, such as snake-like,¹ insect-like,^{2,3} and water-like steps,⁴ have been developed to perform locomotion and complex tasks when externally stimulated. Due to their flexible locomotion and multifunctionality, these bionic

Received: August 31, 2023

Revised: January 4, 2024

Accepted: January 8, 2024

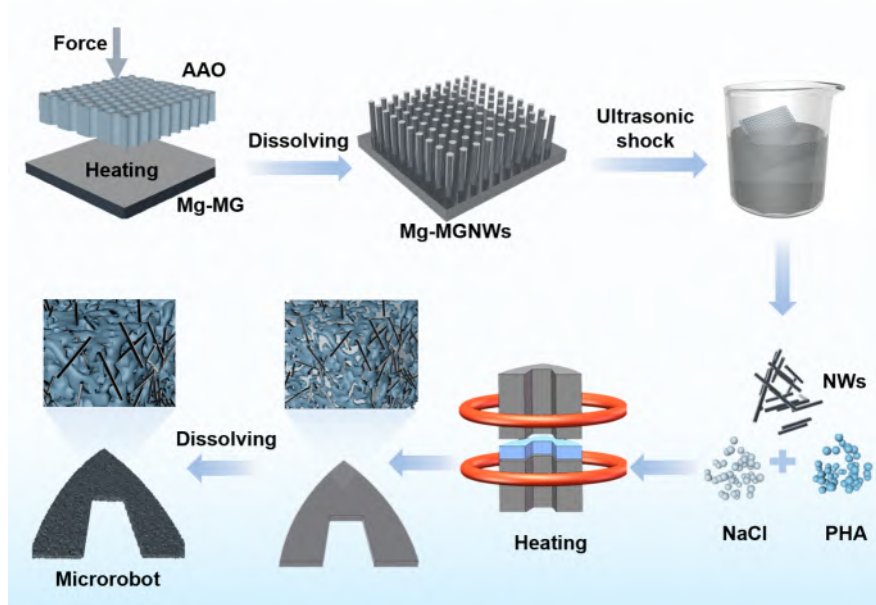


Figure 1. Schematic diagram of microrobot preparation.

robots have wide applications such as cargo transport, power generation,⁵ environmental remediation,^{6,7} and biomedical engineering.⁸ Microrobots that can move efficiently and perform complex and varied tasks on liquid surfaces such as oceans, rivers, and blood have been extensively researched over the past few decades. However, biocompatible robots that can move efficiently in a controlled way for long periods of time and over long distances remain a challenge. To achieve self-driven response, various strategies such as steam propulsion,⁹ the Marangoni effect,^{5,10} catalytic drive,¹¹ magnetism,^{12,13} and light drive^{14–16} were developed. In addition, some researchers have used electric drives to enable robots to move over water.¹⁷ However, the external energy source for these robots is electricity, which always requires a wire connection for power supply. To realize wireless actuation, reagents were added to the end of the robot to form a solution concentration difference. The microrobots can move quickly on the water surface through the surface tension gradient.¹⁸ However, the solution reagents can be discharged into the water, causing negative impacts on the water environment.

Among different driving strategies, light driving of the microrobots based on the Marangoni effect^{5,19,20} is considered an attractive option for moving on liquid surfaces because it is environmentally friendly, efficient, and remotely controllable. According to the Marangoni effect, a temperature change creates a surface tension gradient at the liquid/air interface, and the liquid automatically flows from areas of low surface tension to areas of relatively high surface tension, leading to macroscopic motion of the object.¹⁰ Laser irradiation enables photothermal conversion, leading to local heating of the object and the formation of a surface tension gradient, which enables stimulus-responsive motion in a noncontact telemanipulation method. In order to integrate the photothermal effect into microrobots, extensive research has been conducted on various photothermal materials, including graphene,^{21,22} carbon nanotubes,^{23–25} metallic nanoparticles,^{26–28} and so on. Although the possibility of photothermal surface effects for microrobots has been confirmed by research, microrobots with biocompatible degradability have rarely been investigated.

In this work, a compositional and structural modulation strategy for the preparation of photothermal materials has been proposed. Mg-based metallic glass nanowires (Mg-MGNWs) can be easily prepared through the thermoplastic formation (TPF) method. In addition, the dissolution method for manufacturing porous polyhydroxyalkanoates (PHA) has the advantages of simplicity, convenience, environmental friendliness, and rapidity. Since both Mg-based metallic glass (Mg-MG) and PHA^{29,30} exhibit excellent biocompatibility, a material with excellent photothermal response can be prepared by the combination of nanowires (NWs) with porous PHA structures. Following such a strategy, we used Mg-MG and PHA materials to fabricate biocompatible and degradable photothermal materials using a dissolution fabrication method, which can be applied to light-driven microrobots. The microrobot converts light energy into heat under near-infrared (NIR) laser irradiation through the synergistic effect of the porous PHA structure and localized surface plasmon resonance (LSPR) of NWs. This enables high efficiency and long duration remote control on water surfaces. With a laser power density of 2.0 W/cm², the robot can achieve a speed of up to 9.91 mm/s. After NIR laser irradiation, the microrobot achieves programmable complex motions on the water surface through the Marangoni effect, including straight line, clockwise, counterclockwise, and obstacle avoidance movements. Microrobots have broad application prospects in areas such as drug delivery and liquid detection. This work also provides a reference for the development of biocompatible, degradable, and remotely controlled microrobots.

2. RESULTS AND DISCUSSION

2.1. Preparation and Characterization of Microrobots.

In order to fabricate light-driven microrobots, a compositional and structural preparation strategy for the preparation of photothermal materials has been developed. Porous structures were fabricated by dissolution of NaCl using PHA as the matrix material and Mg-MGNWs as the photothermal enhancement additive. Figure 1 shows the fabrication process of photothermal materials for light-driven microrobots. Initially, Mg-MG was

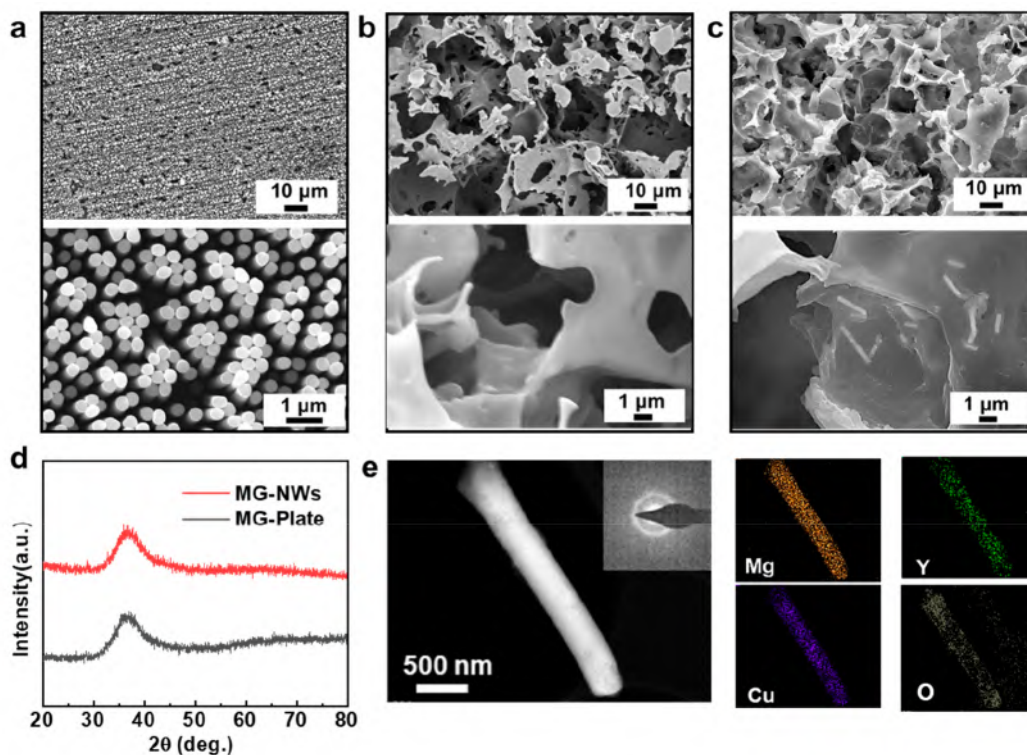


Figure 2. Characterization of microrobots. (a) SEM morphology of Mg-MGNWs. (b) SEM morphology of porous PHA material. (c) SEM morphology of porous PHA/Mg-MGNWs. (d) XRD patterns of Mg-MG. (e) TEM morphology of individual Mg-MGNWs and elemental distribution of Mg-MGNWs, with the inset showing electron diffraction from selected regions.

heated to the supercooled liquid region (SCLR), resulting in the rapid fabrication of large-area NWs on the Mg-MG surface through TPF. The NWs were then collected after being shaken off using ultrasonic vibration and mixed homogeneously with PHA and NaCl powders to create a composite material. Subsequently, the composites were heated in a specially shaped mold, which led to the formation of microrobots with precise shapes and excellent photothermal properties by dissolving the NaCl component in an aqueous solution. Its boat-shaped structure facilitates controlling the direction of motion and reducing drag. For specific dimensions of the microrobot, see Figure S1.

The morphology and characteristics of the prepared NWs are listed in Figure 2a. The average diameter of Mg-MGNWs based on scanning electron microscopy (SEM) image analysis is summarized in Figure S2, and the average diameter of the Mg-MGNWs (~ 309 nm) is consistent with the nanoscale size (~ 306 nm) of the anodic aluminum oxide (AAO) template. By precisely controlling the temperature and pressure of the TPF, the surfaces of the prepared Mg-MGNWs exhibited amorphous structures like the cast Mg-MG plates, as confirmed by the X-ray diffraction (XRD) pattern in Figure 2d. The morphology of individual nanowires under low-resolution transmission electron microscopy (TEM) is shown in Figure 2e, and the selected region electron diffraction pattern in the inset indicates an amorphous surface consistent with the XRD results. Furthermore, the energy spectrum results show a uniform distribution of Mg, Cu, and Y elements in the nanowire without deviation. Figure 2b shows the porous structure prepared using PHA and NaCl, with pore sizes consistent with the original particle size of the NaCl powder used (see Figure S3). Moreover, the detailed image in Figure 2c highlights the presence of Mg-MGNWs in

the formed micropores. This demonstrates the feasibility of compositional and structural modulation strategies for the fabrication of microrobots.

2.2. Photothermal Conversion Performance of Porous PHA/Mg-MGNWs. The photothermal effect of the fabricated porous PHA/Mg-MGNWs is the key concern for light-driven microrobots. The 808 nm NIR laser was chosen to investigate the photothermal conversion performance of the porous PHA/Mg-MGNWs, which is because this wavelength possesses a certain penetration depth and tissue transparency compared with lasers of other wavelengths, making it applicable in the field of biomedical research. The heating mechanism of porous PHA/Mg-MGNWs is shown in Figure 3a. The Mg-MGNWs, as a photothermal material, convert light energy into heat energy through LSPR. At the same time, the porous structure of PHA allows the laser light to be reflected several times inside the holes, which promotes the absorption of light and thus improves its photothermal performance. We performed relevant experiments and simulations on the prepared samples to further validate the microrobot heating mechanism. The N_2 adsorption–desorption isotherm result of the porous PHA/Mg-MGNWs is shown in Figure 3b, with a specific surface area of 5.84 m^2/g . The hysteresis loop closes at a relative pressure of about $P/P_0 = 0.5$, suggesting the presence of mesopores and micropores. The H_3 -type hysteresis loop isotherms do not have any obvious saturated adsorption plateau, suggesting that the pore structure is very irregular. The porous structure allows the laser light to be reflected several times inside the sample, thus promoting photothermal conversion. To understand the heating mechanism of Mg-MGNWs, we performed finite element simulations of the NIR laser absorption properties of Mg-MGNWs using the COMSOL software. The electric field

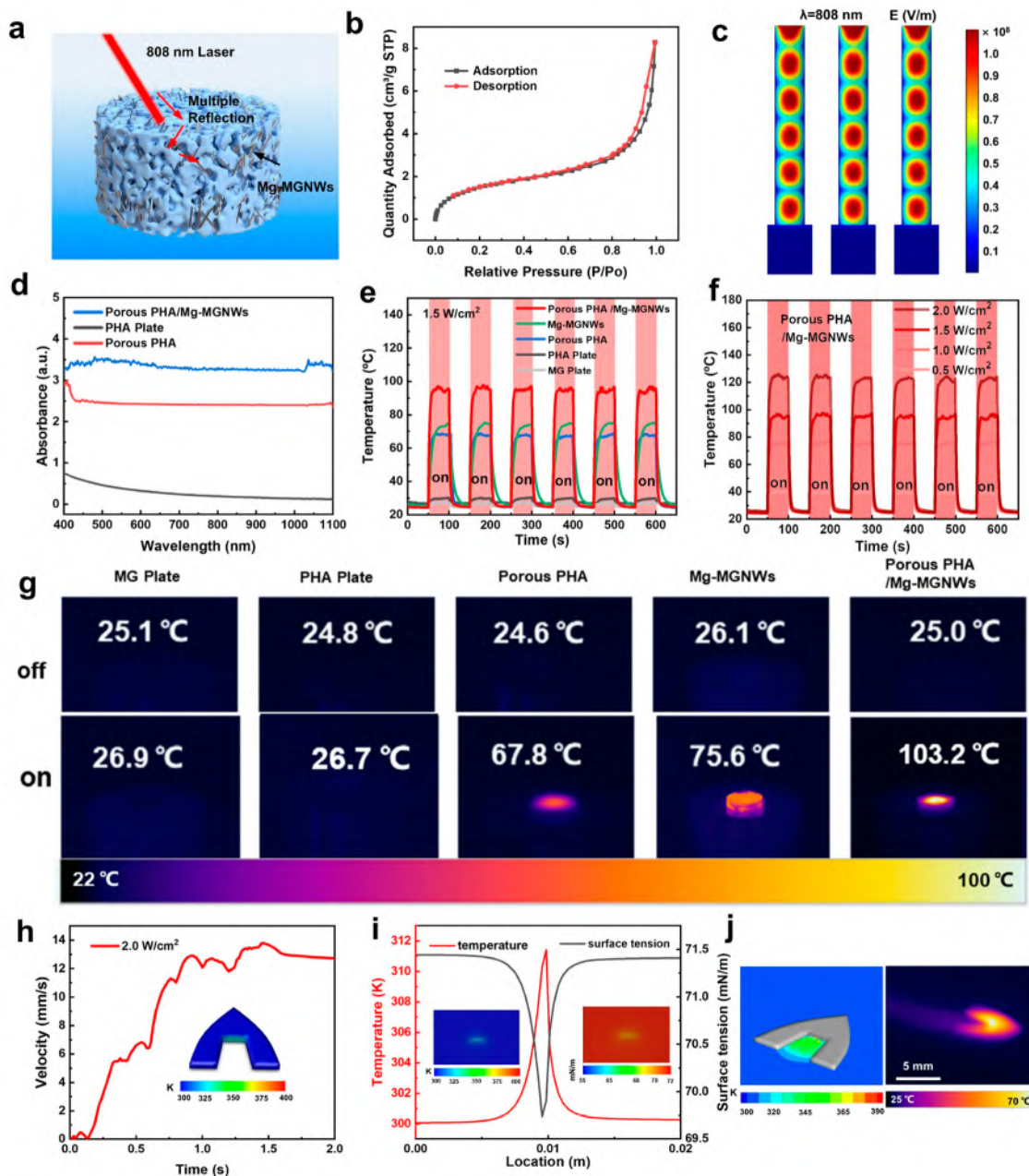


Figure 3. Photothermal conversion performance. (a) Schematic of porous PHA/Mg-MGNWs' heating mechanism. (b) N_2 adsorption and desorption curves of porous PHA/Mg-MGNWs. (c) Electric field distribution at a wavelength of 808 nm. (d) UV–vis–NIR absorption spectra of the PHA plate, porous PHA, and porous PHA/Mg-MGNWs. (e) Temperature curves of MG plate, PHA plate, porous PHA, Mg-MGNWs, and porous PHA/Mg-MGNWs under 1.5 W/cm^2 808 nm NIR laser irradiation. (f) Temperature curves of porous PHA/Mg-MGNWs under different power densities of 808 nm laser irradiation. (g) Infrared images of porous PHA/Mg-MGNWs under laser powers of 0.5, 1.0, 1.5, and 2.0 W/cm^2 . (h) Simulated velocity and corresponding temperature graph of the microrobot. (i) Temperature and surface tension of the water below the microrobot correspondence. (j) Simulated temperature graphs and infrared thermography of a microrobot at the water surface.

distribution of Mg-MGNWs is shown in Figure 3c, which shows the spots on Mg-MGNWs indicate the strength of the light-binding ability. The electric field distribution of the light spots is gradually weakened from the top to the bottom. The laser light is gradually absorbed by the NWs, and the high-density surface LSPR is excited at the hot spot, leading to the absorption of laser light. The light absorption of the PHA plate, porous PHA, and porous PHA/Mg-MGNWs was measured by using UV–vis–NIR spectroscopy. The results in Figure 3d show that the absorbance of porous PHA material increases significantly compared to a PHA plate. In addition, when Mg-MGNWs were

introduced into the porous structure, the light absorption was further enhanced, which is consistent with the measured temperature rise curve effect (Figure 3e). This suggests that the synergistic effect of the porous structure and nanowires can further promote light absorption and thus improve the photothermal effect.

To further analyze the thermal behavior, the temperature rise curves of different samples under NIR laser irradiation with a power density of 1.5 W/cm^2 are shown in Figure 3e. The surface temperatures of MG and PHA plates are only 26.9 and 26.7 °C, respectively, while the surface temperatures of PHA with

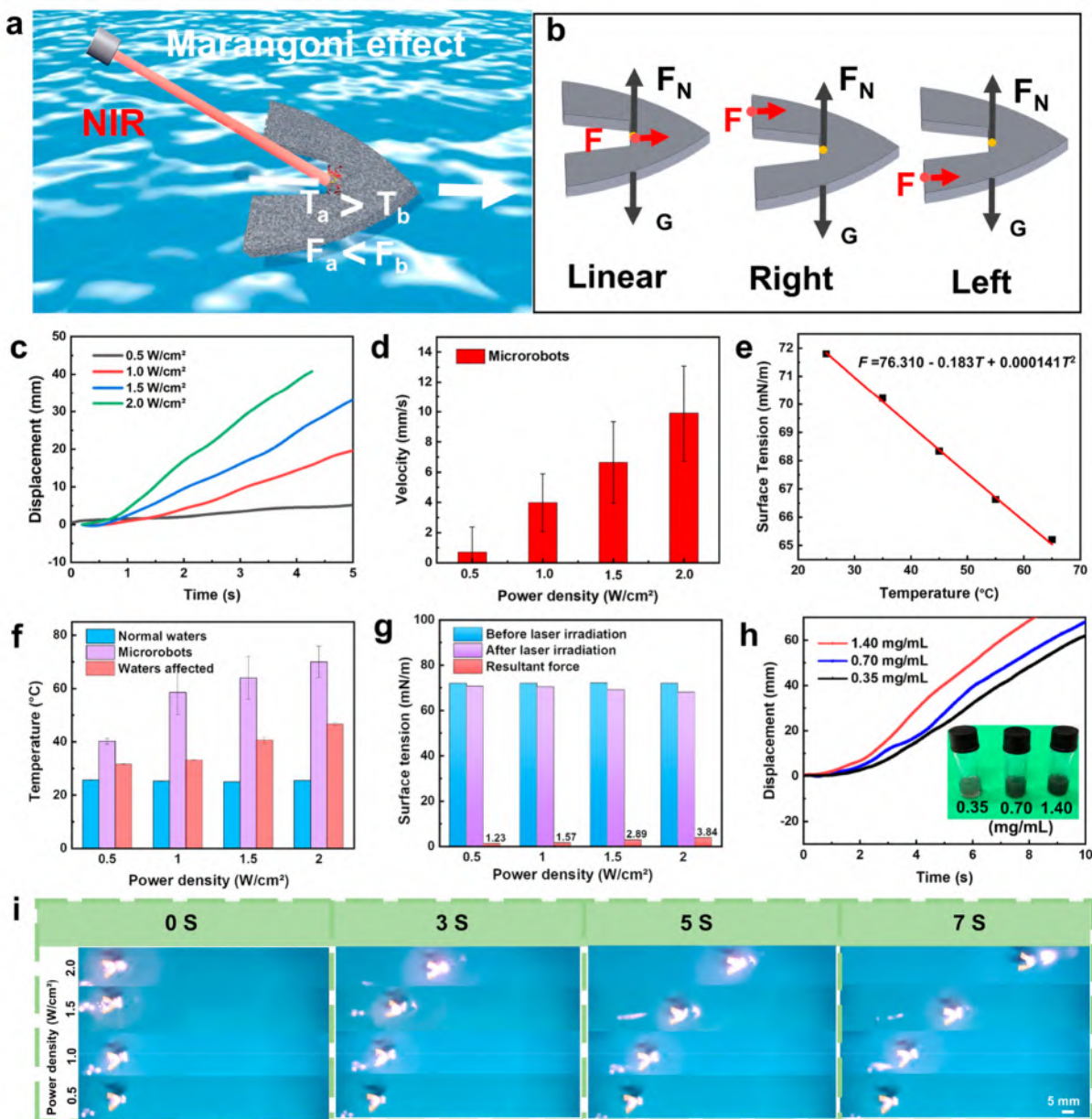


Figure 4. Photothermal drive research for microrobots. (a) Schematic of the microrobot's propulsion based on the Marangoni effect. (b) Force analysis of the microrobot. (c) The displacement curve of the microrobot's movement on the water surface under different power densities. (d) Movement speed of microrobots on the water surface at different power densities. (e) The surface tension of deionized water at different temperatures. (f) Temperature in different areas after laser irradiation. (g) Microrobot driving force on the water surface formed by surface tension. (h) Displacement of microrobots with different concentrations of NWs. (i) Optical image of microrobot motion under different power densities.

microstructures and Mg-MGNWs rapidly increase to 67.8 and 75.6 °C, respectively. Most surprisingly, the highest temperature is then increased to 103.2 °C when porous PHA and Mg-MGNWs are combined. For visual illustration, the corresponding infrared images of the samples with the highest and lowest temperatures are shown in Figure 3g. In addition, the photothermal effect of porous PHA/Mg-MGNW at different power densities (0.5, 1.0, 1.5, and 2.0 W/cm²) was systematically investigated, as shown in Figure 3f, where the temperatures of porous PHA/Mg-MGNW reached 40.3, 75.8, 96.9, and 124.2 °C, respectively. The temperature increase is attributed to multiple emissions within the internal porous structure after laser irradiation, which greatly enhances the optical path

absorption. Furthermore, the high-density LSPR^{31–33} of Mg-MGNWs further elevates the sample temperature. Figure S5 summarizes the heating rate of porous PHA/Mg-MGNWs under different power densities, and the heating rate increases sharply with the power density, reaching a maximum of 26.82 °C/s. These findings validate the rapid and efficient conversion of 808 nm NIR laser energy into thermal energy by porous PHA/Mg-MGNWs. The photothermal effect of porous PHA/Mg-MGNWs provides a basis for microrobots to achieve photothermal drive on the water surface.

In order to better understand the working mechanism of the driving process, ANSYS Fluent software was used to establish a finite element model, and laser power boundary conditions were

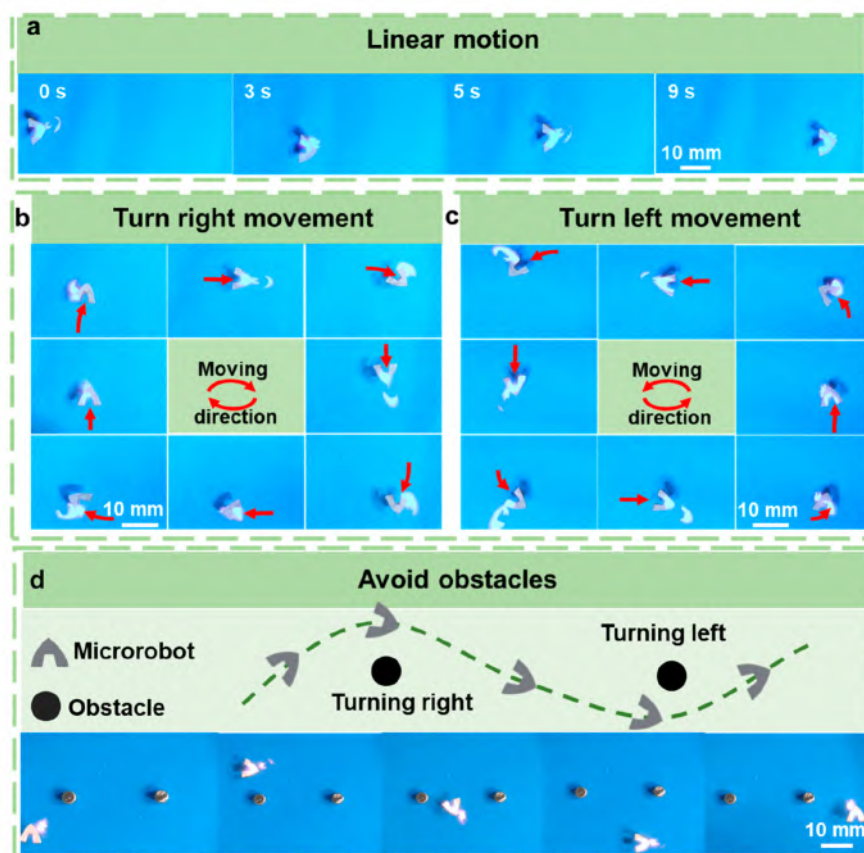


Figure 5. Movement of the light-driven microrobot on the water surface. (a) Optical image showing the linear movement of the microrobot. (b) Clockwise rotation of the microrobot. (c) Counterclockwise rotation of the microrobot. (d) Schematic and optical images demonstrating the obstacle avoidance of the microrobot.

defined for the microrobot. The corresponding transient thermal and velocity analysis is carried out, the microrobot speed increases gradually in 1 s and finally tends to stabilize at about 13 mm/s (Figure 3h), and the temperature and surface tension graphs of the water below the microrobot are obtained according to the quantitative relationship between surface tension and temperature (Figure 3i and Figure S6). There is a surface tension difference between the irradiated and non-irradiated areas, which drives the microrobot from the low surface tension area of the irradiated area to the high surface tension area. Figure 3j shows the simulated motion of the microrobot at the water surface and the actual motion by infrared thermography. For the other local temperature gradient induced thermophoretic force^{9,34} at the end of the robot, it does not drive the microrobot because the direction of the thermophoretic force at the end of the robot is opposite the direction of motion (Figure S7).

2.3. The Effect of Photothermal Drives on Microrobots. The photothermal driving of microrobots is directly related to their motion control and functional applications; therefore, their photothermal driving mechanism and its impact on microrobot movement were investigated. By harnessing the facile formation and complex shaping capabilities of porous PHA/Mg-MGNWs composites, we successfully fabricated a biocompatible and degradable microrobot capable of rapid motion on water. The synergistic effect of Mg-MGNWs and the porous structure enable the microrobot to exhibit excellent photothermal response characteristics. When the microrobot's

end face is irradiated with a NIR laser, the porous structure and Mg-MGNWs convert light energy into heat, resulting in an increase in local water temperature. The increase in the temperature induces the Marangoni effect, which results in a decrease in the surface tension of water as the temperature rises. As shown in Figure 4a, the liquid with higher surface tension automatically pulls the liquid with lower surface tension, creating a driving force that propels the microrobot forward.³⁵ This effect is more obvious in areas with higher water temperatures, as the surface tension of the liquid in those regions is greater. The relationship between the temperature and surface tension of the fluid can be calculated using the Harkins equation:³⁶

$$F = b_0 + b_1T + b_2T^2 \quad (1)$$

where F is the local surface tension (mN/m), the b 's are constants ($b_0 = 76.310$ mN/m, $b_1 = -0.183$ mN/(m \cdot °C), $b_2 = 0.000141$ mN/(m \cdot °C²), and T is the temperature (°C) of the fluid. This formula is used to calculate the relationship between the surface tension of water and the temperature, where the constant term b is an empirical coefficient, obtained by inverting the surface tension of water measured at different temperatures, as shown in Figure 4e.

The structural shape of the microrobot has a certain influence on its programmable motion. To achieve remote control over its motion direction, a boat-shaped structure was specifically designed, as shown in Figure 4b. Under normal conditions, when the microrobot floats on the water surface, it remains

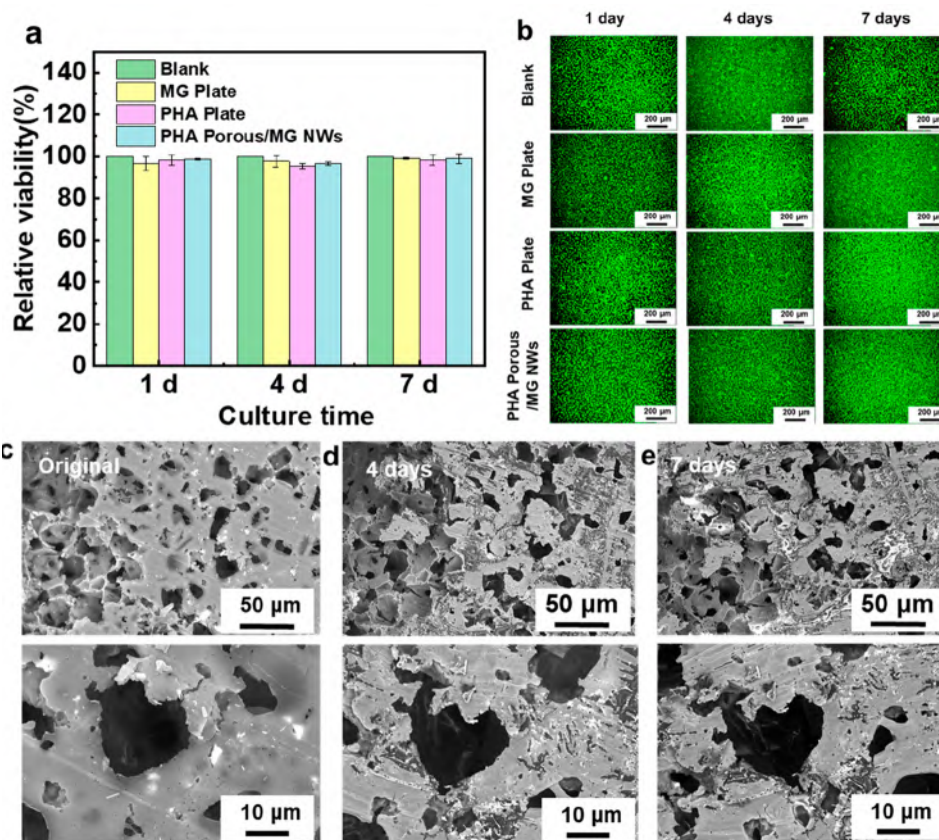


Figure 6. Biocompatibility and degradability. (a) Cell viability of L929 cells cultured with blank, an MG plate, a PHA plate, and porous PHA/Mg-MGNWs for 1, 4, and 7 days ($n = 3$). (b) Fluorescence microscopy images of L929 cells cultured with blank, an MG plate, a PHA plate, and porous PHA/Mg-MGNWs for 1, 4, and 7 days. (c–e) SEM images of porous PHA/Mg-MGNWs after 0, 4, and 7 days of degradation in SBF.

stationary due to balanced surface tensions on both sides. However, when the NIR laser irradiated the side of the microrobot near its center of gravity, it converted light energy to heat, resulting in a surface tension difference that propels the microrobot forward. When the laser irradiates the left and right sides of the microrobot, the surface tension generated does not intersect with the center of gravity. Instead, it creates a torque T at a distance L from the central axis, leading to rotation of the microrobot.

It is worth noting that the speed of movement is also influenced by the laser power density. As the laser power density increases, the heating rate of the microrobot increases, allowing for larger displacements within the same time. As shown in Figure 4c, the displacements achieved by the microrobot driven on the water surface in 4 s under different power densities (0.5, 1.0, 1.5, and 2.0 W/cm²) are 2.40, 12.59, 24.93, and 38.66 mm, respectively. Furthermore, Figure 4d reveals that the average velocity on the water surface also increases with the increase in power density. Figure 4i and Supplementary Video S1 further visualize and compare the variation of the motion speed of the microrobot under different laser power densities, where the microrobot exhibits relatively slow motion under low power density conditions and faster motion under high power density conditions. Under laser irradiation with power densities of 0.5, 1.0, 1.5, and 2.0 W/cm², the corresponding velocities of the microrobot are 0.7, 3.99, 6.65, and 9.91 mm/s, respectively.

In terms of its motion mechanism analysis, the microrobot is mainly influenced by gravity (G), flotation (F_N), and surface tension. When the microrobot is irradiated by a NIR laser on its

side, the surface tension in the irradiated area decreases, resulting in a surface tension difference F .

$$\vec{F} = \vec{F}_b - \vec{F}_a \quad (2)$$

where F_a represents the surface tension after laser irradiation, while F_b represents the surface tension without laser irradiation.

As shown in Figure 4f, the temperature of the microrobot increases under laser irradiation and is transferred to the irradiated water below it by thermal radiation and convection. The temperature of the irradiated water is higher than that of the unirradiated water, resulting in a surface tension difference. According to the above equation, the surface tension difference at different power densities (0.5, 1.0, 1.5, 2.0 W/cm²) is calculated to be 1.23, 1.57, 2.89, and 3.84 mN/m, respectively. As shown in Figure 4g, with the increase of the laser power density, the temperature of the microrobot and the water below it increases, which leads to the increase of the surface tension difference, and the microrobot's speed is increased accordingly. To investigate the effect of the NWs' concentration on the driving speed of the microrobots, we added three different concentrations of NWs (0.35, 0.7, and 1.4 mg/mL) to the microrobots. From Figure 4h, it can be found that the movement speed of the microrobots increases with the increase of NWs' concentration. This is because the increase in the concentration of NWs promotes the photothermal properties, thereby increasing the speed of movement.

In this study, we demonstrate that it is possible to manipulate the motion of a microrobot using lasers to achieve programmable complex motions by controlling the laser irradiation at

different positions. As shown in Figure 5a and Video S2, gravity and flotation are balanced, and the resultant force of surface tension intersects with the center of gravity, thus achieving linear motion. Additionally, to further explore the functionality of the microrobot, we show an optical image of the microrobot rotating in Figure 5b and Video S2. By irradiating the left position of the microrobot with an NIR laser, we successfully achieve clockwise motion. Similarly, by irradiating the laser at the right position, we were able to observe the microrobot rotating counterclockwise, as shown in Figure 5c and Video S2. The realization of these rotational motions provides strong support for the diverse motions of the microrobot. Furthermore, by combining the linear motion and rotational motion of the microrobot, obstacle avoidance functionality can be achieved, as shown in Figure 5d and Video S2. The results indicate that the microrobot composed of porous PHA/Mg-MGNWs can achieve a high efficiency and long-term remote control on water surfaces. This study demonstrates the great potential of the Marangoni effect in object motion manipulation and provides an important reference for the further development of fine manipulation systems and applications. We believe that these findings will have a positive impact on the further development of microrobot technology and related fields.

2.4. Degradable Biocompatibility of Porous PHA/Mg-MGNWs. The biocompatibility and degradability of microrobots are critical considerations for their extensive applications in drug delivery, remote sampling, and biosensors. In order to investigate the response of the prepared porous PHA/Mg-MGNWs composite material on cell viability, the MG plate, PHA plate, and porous PHA/Mg-MGNWs were cultured with mouse fibroblast cells (L929) in the culture medium. The cell viability of cultured L929 cells was examined, as shown in Figure 6a. In the blank group, the relative cell viability remained at 100% for 7 days. The cell viability of the MG plate decreased to 96.6% after 24 h of cultivation and increased to 99.2% after 7 days with the increase of cultivation time, which was attributed to the release of Mg^{2+} from degradation to promote cell growth and multiplication.^{37,38} Similarly, the PHA plate also exhibited a higher cell viability, and the addition of Mg-MGNWs to the porous PHA maintained a cell viability above 96%. The addition of Mg-based Mg-MGNWs is beneficial for early cell diffusion and proliferation, which are fundamental processes for cell growth and differentiation.

For visual assessment of cell vitality and survival, the cells were stained with Calcein fluorescent dye and observed using fluorescence microscopy. As shown in Figure 6b, the MG plate, PHA plate, and porous PHA/Mg-MGNWs exhibited high fluorescence intensity, indicating a high level of cell viability. To evaluate the effects of immersion in simulated body fluid (SBF), the prepared porous PHA/Mg-MGNWs were immersed, and the samples were observed using SEM after 0, 4, and 7 days of immersion, as shown in Figure 6c–e. However, immersion led to the dissolution of MG due to the presence of Cl^- ions and other factors, resulting in the formation of a layered structure. Additionally, PHA gradually degraded, leading to the formation of numerous cracks. The variation of the mass of porous PHA/Mg-MGNWs with time over 7 days in SBF is shown in Figure S8; with the increase of time, the prepared porous PHA/Mg-MGNWs gradually decreased and showed a trend of degradation. The above results indicate that our porous PHA/Mg-MGNWs photothermal materials prepared by using dissolution fabrication have excellent biocompatible and

degradable properties for application in photothermally driven microrobots.

3. CONCLUSIONS

In summary, we propose compositional and structural design strategies to prepare materials with excellent photothermal properties for the preparation of light-driven microrobots with complex shapes. Fabrication of porous structures by dissolving NaCl from Mg-MGNWs and PHA can prepare microrobots with excellent photothermal effects and complex shapes. Under an 808 nm NIR laser with a power of 2 W/cm^2 , the porous PHA/Mg-MGNWs were able to heat up with a heating rate of $26.82 \text{ }^\circ\text{C/s}$ to $124.2 \text{ }^\circ\text{C}$. The excellent photothermal effect was attributed to the trapping of light in its porous structure, multiple reflections of the laser light in the porous structure, and induction of the LSPR by the Mg-MGNWs. Due to the Marangoni effect caused by the temperature difference, the microrobot can realize programmable complex motions such as linear, clockwise, counterclockwise, and obstacle avoidance motions on the water surface. Under a laser irradiation of 2.0 W/cm^2 , a driving force of 7.50 mN can be created to move the microrobot on the water surface at a speed of 9.91 mm/s . Both Mg-MG and PHA possess excellent biocompatibility; therefore, the fabricated microrobots are both biocompatible and degradable. We believe that the strategy of biocompatible and degradable microrobot fabrication has a huge potential for application areas, such as fluid detection, drug transportation, and biomedical diagnostics.

4. EXPERIMENTAL SECTION

4.1. Materials. The $Mg_{65}Cu_{25}Y_{10}$ (at. %) MG was selected in the present work, as it has a wide SCLR, thermal ability, and excellent biocompatibility. The Mg (>99.99% purity) element was added to the Cu–Y intermediate alloy ingot by induction melting to form the final ingot. MG plates with a thickness of 1.5 mm were then obtained by spray casting the molten alloy into a copper mold. The prepared MG plates were cut into small pieces of 5 mm diameter and polished. The PHA powder was purchased from Guangdong Zhonglian Plasticizing Technology Co., Ltd. The NaCl particles were purchased from Shanghai Macklin Biochemical Technology Co., Ltd.

4.2. The Details of TPF. The polished MG plates were placed on the AAO template by using a through hole having a diameter of $\sim 300 \text{ nm}$ in the TPF mold. After heating the sample to its SCLR (see Figure S4) at a 60 K/min heating rate, a constant load of 500 MPa was applied and held for 30 s to force the Mg-MG to fill the nanopores of the AAO template. The pressure was then quickly released, and the specimen was removed from the mold and cooled. Finally, the samples with AAO templates were dissolved in 20 wt % NaOH at a temperature of $60 \text{ }^\circ\text{C}$ for 10 min, after which the samples were washed with ultrapure water to obtain samples of Mg-MGNWs.

4.3. Fabrication of the Microrobot. The Mg-MGNWs prepared by TPF were dispersed into an anhydrous ethanol solution prepared at a concentration of 0.7 mg/mL using ultrasound. After the anhydrous ethanol was evaporated, it was mixed well with PHA and NaCl (PHA:NaCl, 1:3). The mixed powder was filled into a designed microrobot mold and heated at 423 K for 30 min for solidification. After molding, it was removed in an aqueous solution for dissolution to remove NaCl, resulting in the formation of microrobots with a porous structure and NWs.

4.4. Characterization of Multiscale Structures. The amorphous nature of Mg-MG before and after TPF was characterized by XRD equipment (Rigaku MiniFlex600) with Cu $K\alpha$ radiation. The XRD patterns were obtained in the range of scan angles 2θ of $20\text{--}80^\circ$ at a scan rate of $5^\circ/\text{min}$ and a scan interval of 0.02. The thermodynamic properties of Mg-based MGs (glass temperature T_g and crystallization temperature T_x) were investigated by differential scanning calorimetry

(DSC; PerkinElmer DSC-8000) at a continuous heating rate of 20 K/min under a high-purity argon flow. Mg-MGNWs and porous PHA structures were analyzed by field emission SEM (FEI QUANTA FEG 450). The atomic structure was characterized by using JEM-2100 F TEM and energy dispersive spectroscopy. Nitrogen adsorption/desorption experiments were performed using Micromeritics ASAP 2020, and the specific surface area of the samples was calculated using the BET method. Absorbance was measured using a UV-vis-NIR spectrophotometer (Shimadzu UVmini-1280, Japan). Surface tension of deionized water at different temperatures was measured by a surface tension meter (Kruss K100, Germany).

4.5. Photothermal Characterization. The photothermal effect of the sample was characterized using an 808 nm laser (10 W, ZLM10000AD808-100F). The sample was placed on quartz, and the laser switch had a period of 100 s with 6 cycles of irradiation. To capture the thermal response on the sample's surface, an infrared thermal imaging camera (Fotric 280d) was used, with a data acquisition frequency of 1 Hz. Additionally, the motion displacement videos were captured at a frequency of 12 Hz.

4.6. Cell Viability. Cell viability was assessed by using the CCK-8 assay. The control group consisted of 200 μ L per well of complete culture medium and L929 cells. The blank group contained only the culture medium and CCK-8. In the experimental group, L929 cells were treated with the sample extract solution. Mouse fibroblast (L929) cells were seeded onto a 96-well plate (1×10^4 cells/well) and cultured at 37 °C in a 5% CO₂ incubator for 24 h. The medium was then replaced with the extract solution of the samples and continued to be cultured for 1, 4, and 7 days. Following removal of the original culture medium, two washes with PBS (GNM20012; Dr. Bold Bio) were performed. Subsequently, 100 μ L of fresh culture medium containing 10% fetal bovine serum was added to each well, and 10 μ L of a CCK-8 solution was added to each well. After incubating in the incubator for 2 h, the absorbance at 450 nm of each well was measured using a microplate reader (EPOCH2; Biotek). The viability of live cells in the sample extract was visualized and quantified by using the fluorescent dye Calcein, which emits green fluorescence on excitation. Cells were washed twice with PBS and then incubated with 200 μ L of staining working solution in the dark at 4 °C for 15–20 min. The results were then examined by using a fluorescence microscope (Leica DM18).

4.7. Degradability Tests in SBF Solution. The in vitro degradation of the porous PHA/Mg-MGNWs composite material was evaluated through an immersion test. Samples with a diameter of 5 mm were immersed in SBF (pH = 7.4–7.5, purchased from Phygene Biotechnology Co. Ltd. in Fuzhou) for 1, 4, and 7 days. The surface morphology of the porous PHA/Mg-MGNWs after immersion was observed by using SEM.

ASSOCIATED CONTENT

Supporting Information

The Supporting Information is available free of charge at <https://pubs.acs.org/doi/10.1021/acsnano.3c08277>.

Specific dimensions of the microrobot; SEM image of the AAO template and statistical distribution of AAO pore size and Mg-MGNWs diameter; SEM image of NaCl particles and statistical particle size distribution; the DSC curves of Mg-based MG; heating rate at different power densities; temperature field graphs and surface tension fields of the microrobot and the waters; analysis of the thermophoretic force of the microrobot; mass change of porous PHA/Mg-MGNWs; microrobot motion under different power densities; programmable and complex motions of the microrobot (PDF)

Video S1. Microrobot motion under different power densities (MP4)

Video S2. Programmable and complex motions of the microrobot (MP4)

AUTHOR INFORMATION

Corresponding Author

Jiang Ma – State Key Laboratory of Radio Frequency Heterogeneous Integration, College of Mechatronics and Control Engineering, Shenzhen University, Shenzhen 518060, China; orcid.org/0000-0003-0234-3210; Email: majiang@szu.edu.cn

Authors

Jinbiao Huang – State Key Laboratory of Radio Frequency Heterogeneous Integration, College of Mechatronics and Control Engineering, Shenzhen University, Shenzhen 518060, China

Xiangyang Yu – State Key Laboratory of Radio Frequency Heterogeneous Integration, College of Mechatronics and Control Engineering, Shenzhen University, Shenzhen 518060, China

Luyao Li – State Key Laboratory of Radio Frequency Heterogeneous Integration, College of Mechatronics and Control Engineering, Shenzhen University, Shenzhen 518060, China

Wenxue Wang – State Key Laboratory of Radio Frequency Heterogeneous Integration, College of Mechatronics and Control Engineering, Shenzhen University, Shenzhen 518060, China

Heting Zhang – State Key Laboratory of Radio Frequency Heterogeneous Integration, College of Mechatronics and Control Engineering, Shenzhen University, Shenzhen 518060, China

Yu Zhang – State Key Laboratory of Radio Frequency Heterogeneous Integration, College of Mechatronics and Control Engineering, Shenzhen University, Shenzhen 518060, China

Jian Zhu – State Key Laboratory of Radio Frequency Heterogeneous Integration, College of Mechatronics and Control Engineering, Shenzhen University, Shenzhen 518060, China

Complete contact information is available at:

<https://pubs.acs.org/doi/10.1021/acsnano.3c08277>

Author Contributions

Jinbiao Huang: methodology, writing – drafting, review, and editing, investigation, data management. Xiangyang Yu: formal analysis, data management. Luyao Li: formal analysis, writing – reviewing. Wenxue Wang: validation. Heting Zhang: formal analysis. Yu Zhang: visualization. Jian Zhu: formal analysis. Jiang Ma: conceptualization, validation, writing – reviewing and editing, funding acquisition, supervision.

Notes

The authors declare no competing financial interest.

ACKNOWLEDGMENTS

The work was financially supported by the Key Basic and Applied Research Program of Guangdong Province, China (Grant No. 2019B030302010), the National Key Research and Development Program of China (Grant No. 2018YFA0703605), the NSF of China (Grant Nos. 52122105, 51971150), and the Science and Technology Innovation Commission Shenzhen (Grant Nos. RCJC202210-08092730037, 20220804091920001). The authors also thank the Electron Microscope Center of Shenzhen University for the assistance with microscope observations.

REFERENCES

- (1) Wang, M.; Hu, X. B.; Zuo, B.; Huang, S.; Chen, X. M.; Yang, H. Liquid crystal elastomer actuator with serpentine locomotion. *Chem. Commun.* **2020**, *56* (55), 7597–7600.
- (2) Ahn, C.; Liang, X.; Cai, S. Bioinspired Design of Light-Powered Crawling, Squeezing, and Jumping Untethered Soft Robot. *Adv. Mater. Technol.* **2019**, *4* (7), DOI: 10.1002/admt.201900185.
- (3) Zuo, B.; Wang, M.; Lin, B. P.; Yang, H. Visible and infrared three-wavelength modulated multi-directional actuators. *Nat. Commun.* **2019**, *10* (1), 4539.
- (4) Wang, X.; Dai, L.; Jiao, N.; Tung, S.; Liu, L. Superhydrophobic photothermal graphene composites and their functional applications in microrobots swimming at the air/water interface. *Chem. Eng. J.* **2021**, *422*, 129394.
- (5) Liu, C.; Jiang, D.; Zhu, G.; Li, Z.; Zhang, X.; Tian, P.; Wang, D.; Wang, E.; Ouyang, H.; Xiao, M.; et al. A Light-Powered Triboelectric Nanogenerator Based on the Photothermal Marangoni Effect. *ACS Appl. Mater. Interfaces* **2022**, *14* (19), 22206–22215.
- (6) Liang, C.; Zhan, C.; Zeng, F.; Xu, D.; Wang, Y.; Zhao, W.; Zhang, J.; Guo, J.; Feng, H.; Ma, X. Bilayer Tubular Micromotors for Simultaneous Environmental Monitoring and Remediation. *ACS Appl. Mater. Interfaces* **2018**, *10* (41), 35099–35107.
- (7) Gao, Y.; Xiong, Z.; Wang, J.; Tang, J.; Li, D. Light hybrid micro/nano-robots: From propulsion to functional signals. *Nano Res.* **2022**, *15* (6), 5355–5375.
- (8) Huang, X.; Liu, Y.; Feng, A.; Cheng, X.; Xiong, X.; Wang, Z.; He, Z.; Guo, J.; Wang, S.; Yan, X. Photoactivated Organic Nanomachines for Programmable Enhancement of Antitumor Efficacy. *Small* **2022**, *18* (24), No. e2201525.
- (9) Meng, F.; Hao, W.; Yu, S.; Feng, R.; Liu, Y.; Yu, F.; Tao, P.; Shang, W.; Wu, J.; Song, C.; et al. Vapor-Enabled Propulsion for Plasmonic Photothermal Motor at the Liquid/Air Interface. *J. Am. Chem. Soc.* **2017**, *139* (36), 12362–12365.
- (10) Pan, D.; Wu, D.; Li, P. J.; Ji, S. Y.; Nie, X.; Fan, S. Y.; Chen, G. Y.; Zhang, C. C.; Xin, C.; Xu, B.; et al. Transparent Light-Driven Hydrogel Actuator Based on Photothermal Marangoni Effect and Buoyancy Flow for Three-Dimensional Motion. *Adv. Funct. Mater.* **2021**, *31* (14), DOI: 10.1002/adfm.202009386.
- (11) Karshalev, E.; Kumar, R.; Jeerapan, I.; Castillo, R.; Campos, I.; Wang, J. Multistimuli-Responsive Camouflage Swimmers. *Chem. Mater.* **2018**, *30* (5), 1593–1601.
- (12) Wang, X.; Lin, D.; Zhou, Y.; Jiao, N.; Tung, S.; Liu, L. Multistimuli-Responsive Hydroplaning Superhydrophobic Microrobots with Programmable Motion and Multifunctional Applications. *ACS Nano* **2022**, *16* (9), 14895–14906.
- (13) Li, A.; Li, H.; Li, Z.; Zhao, Z.; Li, K.; Li, M.; Song, Y. J. S. a. Programmable droplet manipulation by a magnetic-actuated robot. *Sci. Adv.* **2020**, *6* (7), No. eaay5808.
- (14) Yang, R. L.; Zhu, Y. J.; Qin, D. D.; Xiong, Z. C. Light-Operated Dual-Mode Propulsion at the Liquid/Air Interface Using Flexible, Superhydrophobic, and Thermally Stable Photothermal Paper. *ACS Appl. Mater. Interfaces* **2020**, *12* (1), 1339–1347.
- (15) Su, X.; Li, H.; Lai, X.; Yang, Z.; Chen, Z.; Wu, W.; Zeng, X. Vacuum-assisted layer-by-layer superhydrophobic carbon nanotube films with electrothermal and photothermal effects for deicing and controllable manipulation. *J. Mater. Chem. A* **2018**, *6* (35), 16910–16919.
- (16) Cao, W.-T.; Feng, W.; Jiang, Y.-Y.; Ma, C.; Zhou, Z.-F.; Ma, M.-G.; Chen, Y.; Chen, F. Two-dimensional MXene-reinforced robust surface superhydrophobicity with self-cleaning and photothermal-actuating binary effects. *Mater. Horiz.* **2019**, *6* (5), 1057–1065.
- (17) Yan, J. H.; Zhang, X. B.; Zhao, J.; Liu, G. F.; Cai, H. G.; Pan, Q. M. A miniature surface tension-driven robot using spatially elliptical moving legs to mimic a water strider's locomotion. *Bioinspir. Biomim.* **2015**, *10* (4), 046016.
- (18) Dai, R.; Li, G.; Xiao, L.; Li, Y.; Cui, Z.; Jia, L.; Zhou, M.; Song, Y.; Yang, Y.; Cai, Y.; et al. A droplet-driven micro-surfboard with dual gradients for programmable motion. *Chem. Eng. J.* **2022**, *446*, 136874.
- (19) Xiang, Y.; Li, B.; Li, B.; Bao, L.; Sheng, W.; Ma, Y.; Ma, S.; Yu, B.; Zhou, F. Toward a Multifunctional Light-Driven Biomimetic Mudskipper-Like Robot for Various Application Scenarios. *ACS Appl. Mater. Interfaces* **2022**, *14* (17), 20291–20302.
- (20) Shi, Y.; Wang, D.; Xiao, Y.; Pan, T.; Lu, D.; Zhu, G.; Xiong, J.; Li, B.; Xin, H. Light-Induced Cold Marangoni Flow for Microswarm Actuation: From Intelligent Behaviors to Collective Drug Delivery. *Laser Photonics Rev.* **2022**, *16* (12), DOI: 10.1002/lpor.202200533.
- (21) Yang, M.; Yuan, Z.; Liu, J.; Fang, Z.; Fang, L.; Yu, D.; Li, Q. Photoresponsive Actuators Built from Carbon-Based Soft Materials. *Adv. Opt. Mater.* **2019**, *7* (16), DOI: 10.1002/adom.201900069.
- (22) Hu, Y.; Wu, G.; Lan, T.; Zhao, J.; Liu, Y.; Chen, W. A Graphene-Based Bimorph Structure for Design of High Performance Photoactuators. *Adv. Mater.* **2015**, *27* (47), 7867–7873.
- (23) Zhang, M.; Ban, D.; Xu, C.; Yeow, J. T.-W. J. A. n. Large-Area and Broadband Thermoelectric Infrared Detection in a Carbon Nanotube Black-Body Absorber. *ACS Nano* **2019**, *13*, 13285.
- (24) Zhao, Y.; Zhao, T.; Cao, Y.; Sun, J.; Zhou, Q.; Chen, H.; Guo, S.; Wang, Y.; Zhen, Y.; Liang, X. J.; et al. Temperature-Sensitive Lipid-Coated Carbon Nanotubes for Synergistic Photothermal Therapy and Gene Therapy. *ACS Nano* **2021**, *15* (4), 6517–6529.
- (25) Han, B.; Zhang, Y.-L.; Chen, Q.-D.; Sun, H.-B. Carbon-Based Photothermal Actuators. *Adv. Funct. Mater.* **2018**, *28* (40), DOI: 10.1002/adfm.201802235.
- (26) Fu, J.; Li, Z.; Li, X.; Sun, F.; Li, L.; Li, H.; Zhao, J.; Ma, J. Hierarchical porous metallic glass with strong broadband absorption and photothermal conversion performance for solar steam generation. *Nano Energy* **2023**, *106*, 108019.
- (27) Liu, J. A.-C.; Gillen, J. H.; Mishra, S. R.; Evans, B. A.; Tracy, J. B. J. S. a. Photothermally and magnetically controlled reconfiguration of polymer composites for soft robotics. *Sci. Adv.* **2019**, *5* (8), No. eaaw2897.
- (28) Tan, M. W. M.; Bark, H.; Thangavel, G.; Gong, X.; Lee, P. S. Photothermal modulated dielectric elastomer actuator for resilient soft robots. *Nat. Commun.* **2022**, *13* (1), 6769.
- (29) Koller, M. Biodegradable and Biocompatible Polyhydroxyalkanoates (PHA): Auspicious Microbial Macromolecules for Pharmaceutical and Therapeutic Applications. *Molecules* **2018**, *23* (2), 362.
- (30) Guo, W.; Yang, K.; Qin, X.; Luo, R.; Wang, H.; Huang, R. Polyhydroxyalkanoates in tissue repair and regeneration. *Eng. Regener.* **2022**, *3* (1), 24–40.
- (31) Li, M.; Shi, M.; Wang, B.; Zhang, C.; Yang, S.; Yang, Y.; Zhou, N.; Guo, X.; Chen, D.; Li, S.; et al. Quasi-Ordered Nanoforests with Hybrid Plasmon Resonances for Broadband Absorption and Photodetection. *Adv. Funct. Mater.* **2021**, *31* (38), DOI: 10.1002/adfm.202102840.
- (32) Huang, J.; Fu, J.; Li, L.; Ma, J. Mg-based metallic glass nanowires with excellent photothermal effect. *Scr. Mater.* **2023**, *222*, 115036.
- (33) Fu, J.; Li, X.; Li, Z.; Sun, F.; Wen, W.; Zhao, J.; Ruan, W.; Ren, S.; Zhang, Z.; Liang, X.; et al. Strong absorption in ultra-wide band by surface nano engineering of metallic glass. *Fundam. Res.* **2022**, DOI: 10.1016/j.fmre.2022.09.017.
- (34) Wu, Z.; Si, T.; Gao, W.; Lin, X.; Wang, J.; He, Q. Superfast Near-Infrared Light-Driven Polymer Multilayer Rockets. *Small* **2016**, *12* (5), 577–582.
- (35) Pena-Francesch, A.; Giltinan, J.; Sitti, M. Multifunctional and biodegradable self-propelled protein motors. *Nat. Commun.* **2019**, *10* (1), 3188.
- (36) Wang, W.; Liu, Y.-Q.; Liu, Y.; Han, B.; Wang, H.; Han, D.-D.; Wang, J.-N.; Zhang, Y.-L.; Sun, H.-B. Direct Laser Writing of Superhydrophobic PDMS Elastomers for Controllable Manipulation via Marangoni Effect. *Adv. Funct. Mater.* **2017**, *27* (44), DOI: 10.1002/adfm.201702946.
- (37) Yu, X.; Huang, W.; Zhao, D.; Yang, K.; Tan, L.; Zhang, X.; Li, J.; Zhang, M.; Zhang, S.; Liu, T.; et al. Study of engineered low-modulus Mg/PLLA composites as potential orthopaedic implants: An in vitro and in vivo study. *Colloids Surf., B* **2019**, *174*, 280–290.
- (38) Wang, T.; Lin, C.; Batalu, D.; Zhang, L.; Hu, J.; Lu, W. In vitro study of the PLLA-Mg65Zn30Ca5 composites as potential biodegrad-

able materials for bone implants. *J. Magnesium Alloys* **2021**, *9* (6), 2009–2018.